Research Article

Simultaneous growth of carbon nanotubes on inner/outer surfaces of porous polyhedra: Advanced sulfur hosts for lithium-sulfur batteries

Hengyi Lu[1,2], Chao Zhang[1], Youfang Zhang[2], Yunpeng Huang[2], Mingkai Liu[3] (✉), and Tianxi Liu[1,2] (✉)

[1] State Key Laboratory for Modification of Chemical Fibers and Polymer Materials, College of Materials Science and Engineering, Innovation Center for Textile Science and Technology, Donghua University, 2999 North Renmin Road, Shanghai 201620, China

[2] State Key Laboratory of Molecular Engineering of Polymers, Department of Macromolecular Science, Fudan University, 220 Handan Road, Shanghai 200433, China

[3] School of Chemistry and Chemical Engineering, Jiangsu Key Laboratory of Green Synthetic Chemistry for Functional Materials, Jiangsu Normal University, Xuzhou 221116, China

ABSTRACT

Metal-organic framework (MOF)-derived functional carbon matrices have recently attracted considerable attention as energy-storage materials. However, the development of MOF-derived carbon materials with hierarchical structures, capable of thoroughly preventing the "shuttling" of polysulfides, is still a major challenge. Herein, we synthesized cobalt nanoparticle-containing porous carbon polyhedra with *in situ* grown N-doped carbon nanotube (CNT) backbone (NCCNT-Co), using zeolitic imidazolate framework-67 (ZIF-67) as starting material. The obtained NCCNT-Co, with interconnected N-doped CNTs on both inner and outer surfaces, possesses an integrated conductive network, which can further accelerate the transport of electrons/ions inside the whole sulfur cathode. The mesoporous structure derived from the ZIF-67 matrix and the densely immobilized CNTs, coupled with the homogeneously doped N atoms and Co nanoparticles, can efficiently trap lithium polysulfides (LiPSs) by physical confinement and chemical interactions. Furthermore, the hierarchical structure of the porous carbon polyhedra enables a high sulfur loading of up to 76 wt.% and can also buffer the volume changes of active sulfur during the lithiation process. As a result, the NCCNT-Co-S cathode delivers a high initial specific capacity of 1,300 mAh·g^{-1} at 0.1 C, along with a high capacity of 860 mAh·g^{-1} after 500 cycles at 1 C, with an extremely low capacity decay of 0.024% per cycle.

1 Introduction

Ever-increasing environmental concerns worldwide call for the development of high-performance and low-cost electrochemical energy storage systems [1]. Lithium-sulfur (Li-S) batteries, with naturally abundant

Address correspondence to Mingkai Liu, liumingkai@jsnu.edu.cn; Tianxi Liu, txliu@fudan.edu.cn or txliu@dhu.edu.cn

elemental sulfur as active material, are among the most promising energy storage systems, with a high theoretical energy density of 2,600 Wh·kg^{-1} [1, 2]. Despite their unique advantages, several key issues greatly limit the practical applications of Li-S batteries: (i) the insulating properties of elemental sulfur and intermediate Li$_2$S$_n$ ($n \leq 2$) species, which are present during the charge/discharge process, cause incomplete utilization of the active materials and capacity fading [3]; (ii) the dissolution of Li$_2$S$_n$ ($4 \leq n < 8$) intermediates in the electrolytes causes irreversible loss of active material and decrease of actual capacity [4–6]; (iii) the high volume expansion and contraction of the cathodes during cycling lead to the collapse of the cathode materials, with rapid performance decay [7–9].

Many efforts have been devoted to overcome these issues. Composing sulfur with carbonaceous materials is an attractive method, since the conductive carbon materials not only increase the electrical conductivity of the cathode, but also physically entrap lithium polysulfides (LiPSs) during the charging/discharging processes [1, 3, 10, 11]. For instance, graphene, carbon nanotubes (CNTs), graphitic carbons, and their hybrids have been used in Li-S batteries [12–15]. Peng et al. prepared a graphene/CNT@porous carbon hybrid through the chemical vapor deposition (CVD) process, followed by chemical activation. When used as sulfur host, the all-carbon hybrid containing micro- and mesopores can limit the shuttle phenomenon and achieve a low capacity decay of 0.12% per cycle [12]. However, LiPSs generally dissolve into the electrolyte and diffuse out of the cathode after several initial cycles, due to the weak intermolecular interactions with nonpolar carbon. Recent studies have focused on sulfur hosts exhibiting strong chemical interactions with LiPSs, such as heteroatom-doped carbon [16–19], metal oxides [20, 21], metal sulfides [22], conducting polymers [23, 24], and MXenes [25]; a few approaches for increasing the cycling stability have been developed [1, 26]. As a newly emerging class of functional materials, metal-organic framework (MOF)-derived porous carbons, which contain uniformly distributed metal/metal oxide nanoparticles and N-doped sites, are the subject of extensive studies in various energy-related areas. Moreover, most studies based on MOF-derived carbon cathodes focus on the utilization of

the simple carbonization products of MOFs or their physical mixtures with other carbon-based materials (e.g., graphene) as sulfur hosts [2, 27–31]. Developing novel MOF-derived carbon matrices with rational nanostructures (especially hollow structures) in order to achieve excellent electrochemical performance is still a major challenge.

Nanoparticles of transition metals such as Co, Fe, and Ni can efficiently catalyze the growth of CNTs with appropriate carbon precursors [32, 33]. Taking into account the coexistence of cobalt catalysts and sufficient amounts of carbon precursors (organic linkers such as imidazole) within zeolitic imidazolate frameworks (ZIFs), herein we design and synthesize cobalt nanoparticle-containing porous carbon polyhedra with an N-doped CNT backbone (NCCNT-Co). These materials were obtained using only ZIF-67 as starting material, and then applied as unique sulfur hosts for Li-S batteries. As shown in Fig. 1, the ZIF-67 precursor serves as source of both C and N for N-doped CNTs and as self-template for the polyhedron structure [34]. During the annealing process, Co ions are reduced to metallic Co by H$_2$, and the obtained metallic Co catalyzes the growth of CNTs under a carbon-containing gas atmosphere, generated by the pyrolysis of organic linkers. The fast decomposition of organic linkers and the gradual consumption of carbon by the
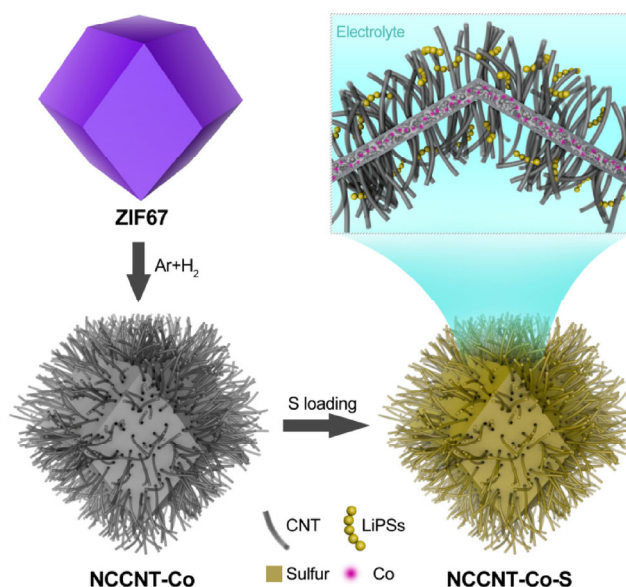

Figure 1 Preparation process of NCCNT-Co-S and schematic illustration of its LiPSs-trapping effect.

growing CNTs take place simultaneously, leading to the formation of the internal hollow morphology. The obtained NCCNT-Co retains a well-defined polyhedral structure, with dense CNT arrays rooted from both the inner and outer surfaces of the polyhedron. The *in situ* grown N-doped CNT arrays form an integrated conductive network, which can efficiently trap LiPSs and prevent their dissolution into the electrolytes; in addition, the hollow structure ensures an efficient interfacial contact between active sulfur and electrolyte, which is beneficial for the rapid conversion reactions of sulfur. The obtained NCCNT-Co-S cathode with high sulfur content (76 wt.%) delivers an extraordinary electrochemical performance, including a high initial capacity of 1,300 mAh·g⁻¹ (at 0.1 C), and a retained capacity of 860 mAh·g⁻¹ after 500 cycles (at 1 C), corresponding to a fading rate of only 0.028% per cycle.

2　Experimental

2.1　Preparation of ZIF-67

In a typical synthesis, 2-methylimidazole (16 mmol) was dissolved in methanol (100 mL) to form solution A, and $Co(NO_3)_2 \cdot 6H_2O$ (4 mmol) was dissolved in another methanol aliquot (100 mL) to form solution B. The two solutions were then mixed under continuous stirring for 10 s, and the final solution was kept for 20 h at room temperature. The purple precipitate was collected by centrifugation at 8,000 rpm, and then washed with methanol for several times, followed by drying at 80 ℃ in vacuum.

2.2　Preparation of NCCNT-Co and NC-Co

ZIF-67 was dispersed in a ceramic boat and heated to 500 ℃ at a heating rate of 2°·min⁻¹ under Ar (50 sccm) atmosphere. Once the temperature reached 500 ℃, H_2 (5 sccm) was introduced in the furnace and held for different times (15, 30, 60 min) before being removed. The system was then kept at 500 ℃ for another 2 h and cooled down to room temperature naturally. The obtained black powder was treated in a 0.5 M H_2SO_4 solution for 6 h. Acid leaching of the carbonization products can remove the unstable Co nanoparticles, decrease the mass density, and further increase the

porosity, thus resulting in a higher specific surface area. The resulting products were collected by centrifugation and repeatedly washed with deionized (DI) water before being dried at 80 ℃. As a reference sample, an NC-Co material was prepared following the same procedure, without the introduction of H_2.

2.3　Preparation of NCCNT-Co-S and NC-Co-S

Active sulfur was encapsulated into NCCNT-Co and NC-Co matrices according to a melt-diffusion method. Typically, the NCCNT-Co or NC-Co matrix was mixed with elemental sulfur in a weight ratio of 1:4, followed by heating at 180 ℃ for 12 h in a tube furnace in a sealed Teflon vessel in Ar. Then, the obtained NCCNT-Co-S and NC-Co-S hybrids were heated at 210 ℃ under flowing Ar for 10 min to vaporize the sulfur deposited on the external surface of the NCCNT-Co and NC-Co matrices.

2.4　Materials characterization

Transmission electron microscopy (TEM) measurements were conducted on a Tecnai G2 20 Twin instrument under an accelerating voltage of 200 kV. Field emission scanning electron microscopy (FESEM) measurements were performed using a Zeiss Ultra 55 instrument at an accelerating voltage of 5 kV. X-ray diffraction (XRD) measurements were carried out using a PANalytical X'pert Pro diffractometer with Cu Kα radiation (operating voltage, 40 kV; cathode current, 40 mA; λ = 0.1542 nm; scan rate, 5°·min⁻¹). X-ray photoelectron spectroscopy (XPS) spectra were collected using a VG Escalab 220I-XL device. The specific surface area and pore size distribution of NCCNT-Co and NC-Co were characterized by N_2 physisorption at 77 K with a Belsorp-max surface area analyzer (Tristar 3000). Thermogravimetric analysis (TGA) was performed to measure the sulfur content, using a TA 50 instrument at a heating rate of 15 ℃·min⁻¹ from room temperature to 800 ℃, under an ultrapure N_2 atmosphere. Raman spectra were obtained on a LabRam-1B French Dilor Com spectrometer (λ = 532 nm).

2.5　Electrochemical measurements

The working electrodes of the NCCNT-Co-S and NC-Co-S materials and pure S were prepared by

mixing NCCNT-Co, NC-Co, and elemental S, respectively, with carbon black and poly(vinylidene fluoride) (PVDF) binder at a 80:10:10 weight ratio in N-methylpyrrolidone (NMP) solvent, to form slurries. The slurries were coated onto aluminum foils and dried at 50 °C for 24 h. A two-electrode system was prepared by inserting a polypropylene film (Celgard 2300) between the working electrode and lithium foil. Lithium bis(trifluoromethanesulfonyl)imide (LITFSI, 1 M) dissolved in dimethoxyethane/1,3-dioxolane (DME/DOL, 1:1 by volume) solution was used as the electrolyte, with 0.5 M LiNO$_3$ as additive. The cells were assembled in an Ar-filled glove box. Cyclic voltammetry (CV) curves were obtained on an Arbin BT2000 system from 1.8 to 3.0 V, at a sweep rate of 0.1 mV·s^{-1}. Charge/discharge tests were performed on a Land CT2001A instrument in a voltage range from 1.8 to 3.0 V. Electrochemical impedance spectroscopy (EIS) measurements were performed on a Solartron analysis system (SI 1260/SI 1287) in the frequency range from 100 kHz to 0.01 Hz. The specific capacities of the assembled cells were calculated based on the weight of sulfur. The areal sulfur loading was 5.2 mg·cm^{-2} and an electrolyte/sulfur ratio of 3:1 was used in the cell fabrication.

3   Results and discussion

The ZIF-67 precursor, with size between 500 and 800 nm, possesses a well-defined polyhedral structure (Fig. S1 in the Electronic Supplementary Material (ESM)). Figures 2(a) and 2(b) show that the direct carbonization of ZIF-67 produces solid porous carbon polyhedra containing Co (NC-Co) with an initial polyhedral shape and a smooth surface.

The TEM images in Fig. 2(c) show that uniformly distributed cobalt nanoparticles with an average size of 5–10 nm are encapsulated within the solid framework. In the case of NCCNT-Co, well-shaped polyhedra are covered with CNTs (Figs. 2(d) and 2(e)); the time for the H$_2$ treatment of 30 min is optimized to obtain designed structures of hollow carbon polyhedron matrix with dense CNT arrays rooted on surface (Fig. S2 in the ESM and Fig. 3).
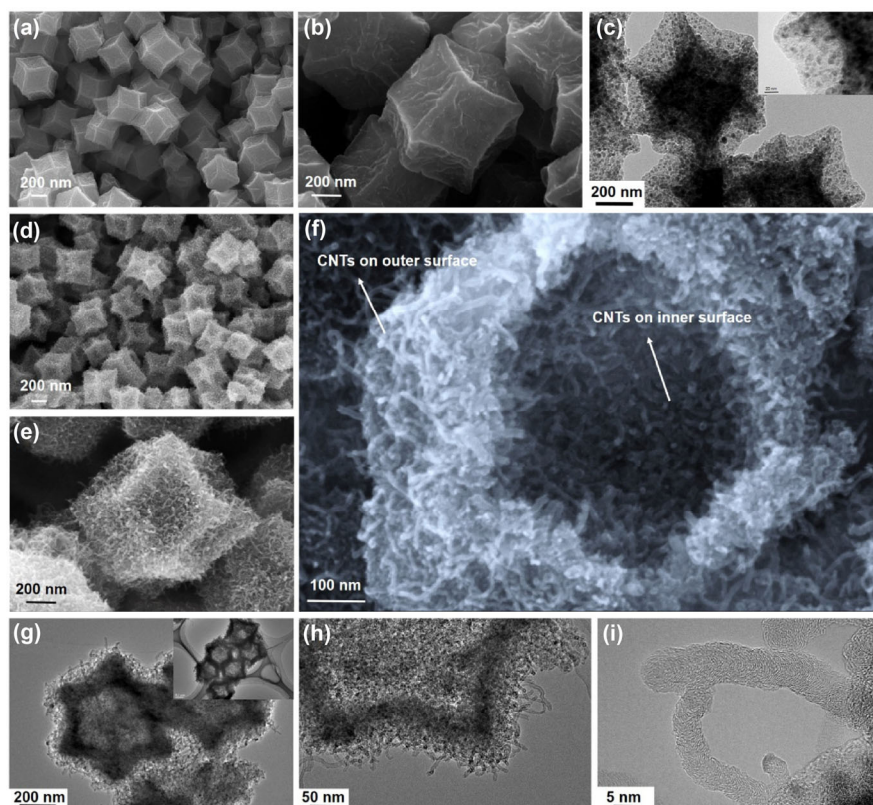

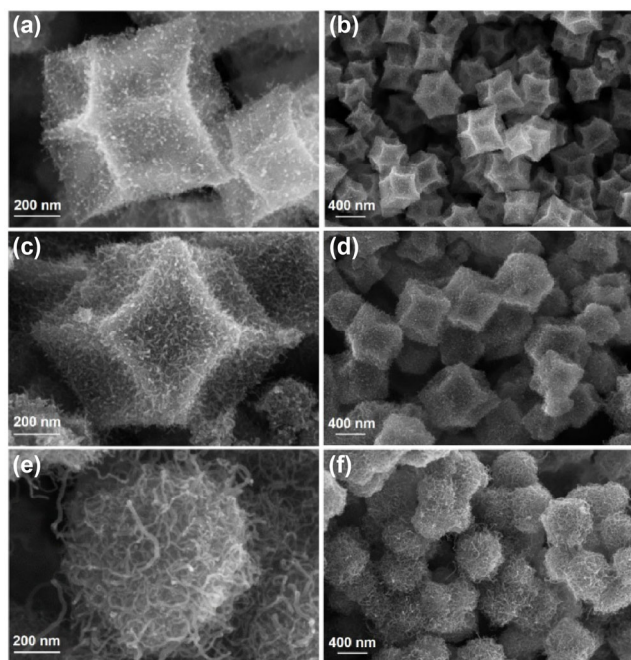**Figure 2**   SEM and TEM images of (a)–(c) NC-Co, and (d)–(i) NCCNT-Co.

Figure 3 High- (left) and low- (right) magnification FESEM images of NCCNT-Co obtained for different H_2 treatment times (a) and (b) 15 min, (c) and (d) 30 min, (e) and (f) 60 min.

Upon increasing the H_2 treatment time to 60 min, the structure of the obtained materials changes into spheres composed of CNTs (Figs. 3(e) and 3(f)). As shown in Fig. S2 in the ESM, the whole carbonization process of ZIF-67 takes 60 min at 500 °C; that is, the growth process of CNTs will last 60 min if hydrogen is continuously fed. As discussed in the Introduction, the growth of CNTs consumes carbon sources generated by the decomposition of the precursor. Therefore, when the H_2 treatment time reaches a certain length, all precursors will be converted into CNTs, leading to the collapse of the polyhedron template and the formation of the final sphere morphology. The FESEM image of the NCCNT-Co sample with a broken shell (Fig. 2(f)) clearly reveals its hollow structure. It is interesting to note that dense CNTs are also observed on the inner surface of the material. The length of the CNTs ranges from dozens to hundreds of nanometers; moreover, the CNTs are connected to each other and show a good distribution, without any aggregation. The TEM image (Fig. 2(g)) further confirms the internal hollow structure of NCCNT-Co. Many interconnected CNTs bridge adjacent NCCNT-Co nanoparticles, ensuring fast electron transfer among different individual polyhedra. The microstructure of

NCCNT-Co was further investigated by high-resolution TEM (HRTEM, Figs. 2(h) and 2(i)). Figure 2(h) reveals that NCCNT-Co is composed of a mesoporous carbon matrix with CNTs rooted on it, and the thickness of the shell is around 100 nm. Moreover, numerous Co nanoparticles with a size between 5 and 10 nm are encapsulated within the mesoporous carbon matrix and the CNT tips. It is interesting to note that the graphitic layers of the CNTs are not completely parallel, indicating the existence of abundant defect sites caused by N-doping, which is beneficial for the electrochemical properties [35, 36].

The XRD patterns (Fig. 4(a)) further confirm the presence of metallic Co in both NCCNT-Co and NC-Co. In addition, the diffraction peak at $2\theta = 26.1°$ of NCCNT-Co is ascribed to the (002) plane of the CNTs. The nitrogen adsorption analysis (Fig. 4(b)) reveals that NCCNT-Co has a larger Brunauer–Emmett–Teller (BET) surface area (653 $m^2 \cdot g^{-1}$) and pore volume (2.06 $mL \cdot g^{-1}$) than NC-Co (361 $m^2 \cdot g^{-1}$ and 0.56 $mL \cdot g^{-1}$, respectively), indicating an integrated structure with additional pores created by the intertwined CNTs. The pore size distributions obtained by the Barrett-Joyner-Halenda (BJH) method reveal that, although large numbers of micropores/mesopores are created in both NCCNT-Co and NC-Co, NCCNT-Co possesses a broader pore distribution and can thus achieve a more efficient restriction of LiPSs. The XPS results confirm the successful N-doping of NCCNT-Co and NC-Co (Figs. 4(c)–4(f)). The electronegative N-doping sites in carbon lattices induce an asymmetric charge distribution and therefore create binding sites for LiPSs, resulting in full utilization of sulfur [37, 38]. The high-resolution Co $2p_{3/2}$ spectra (Fig. 4(f)) reveal the occurrence of metallic Co and N-coordinated Co^{2+} (Co-N) [39]. The metallic Co catalyst can convert the LiPSs deposits back to soluble long-chain LiPSs, and further catalyze the conversion of long-chain LiPSs to Li_2S_2/Li_2S, which may significantly enhance the reaction kinetics, while at the same time leading to a high specific capacity [2, 40]. These results indicate that the NCCNT-Co material, with high N content and uniformly dispersed metallic Co nanoparticles, can serve as conductive matrix promoting the electro-chemical reactions of the cathode at the molecular level. Raman tests were performed to investigate the
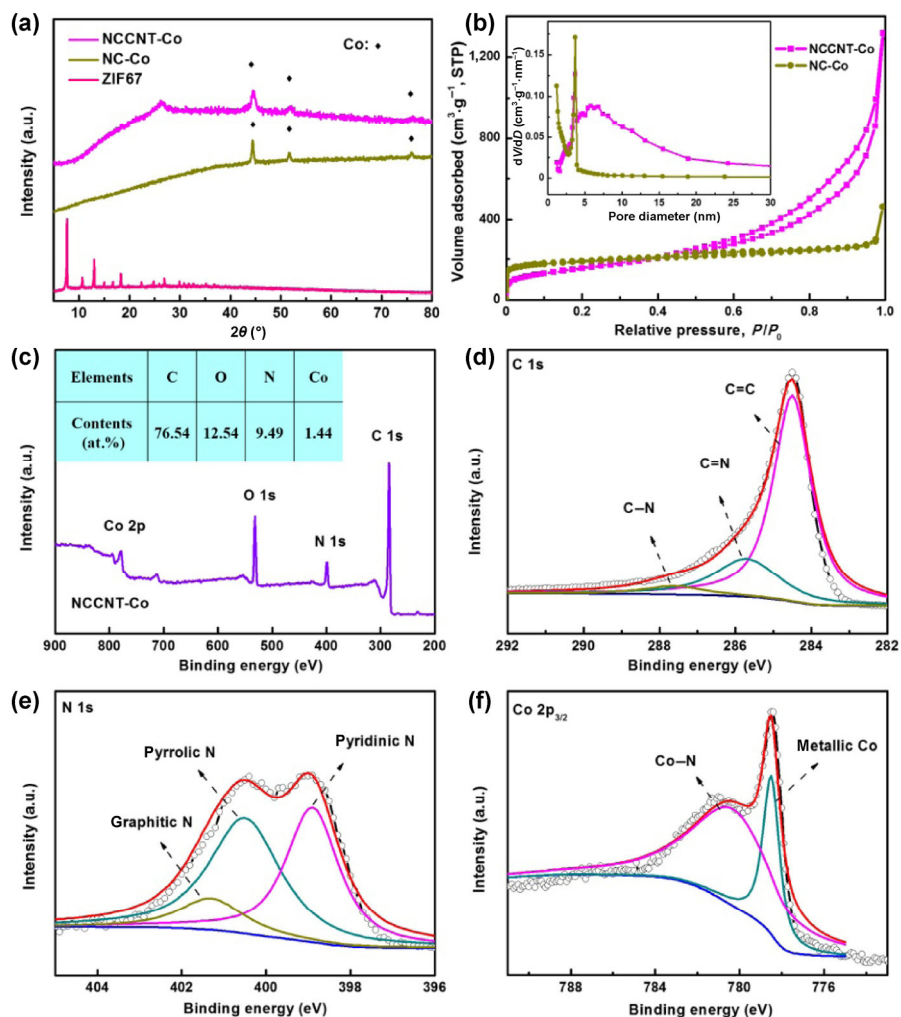
Figure 4 (a) XRD patterns of ZIF-67, NCCNT-Co, and NC-Co. (b) Nitrogen adsorption/desorption isotherms and pore size distribution of NCCNT-Co and NC-Co. (c) XPS survey spectrum of NCCNT-Co. (d)–(f) High-resolution XPS spectra of C 1s, N 1s, and Co $2p_{3/2}$ regions.

graphitization degree of NCCNT-Co and NC-Co. As shown in Fig. S3 in the ESM, both NCCNT-Co and NC-Co spectra show the peaks attributed to the D and G bands, which correspond to defective and graphitic carbon, respectively. The lower I_D/I_G ratio of NCCNT-Co indicates a higher graphitization degree, which translates into a higher conductivity.

NCCNT-Co-S and NC-Co-S composites were prepared by impregnating sublimed sulfur into the hosts via a melt-diffusion method. The SEM images in Figs. 5(a) and 6(a) indicate that both composites maintain their original morphology, with no evident sulfur aggregation on their surface, showing that all sulfur has been encapsulated within the polyhedra. The scanning TEM (STEM) image and the corres-

ponding elemental mappings of NCCNT-Co-S (Figs. 5(b)–5(f)) reveal that the hollow structure of NCCNT-Co is well retained after the sulfur impregnation. Moreover, the homogeneous dispersion of C, Co, N, and S elements indicates that sulfur is located in the pores of the hollow carbon polyhedron matrix rather than within the inner voids, in bulk form. Figures 6(b)–6(f) show the STEM image and homogeneous distributions of C, Co, N, and S elements in NC-Co-S. The XRD patterns of NCCNT-Co-S and NC-Co-S (Fig. 5(g)) exhibit the characteristic diffraction peaks of neat sulfur, further confirming the successful incorporation of sulfur. The sulfur contents in NCCNT-Co-S and NC-Co-S were measured by TGA under nitrogen atmosphere (Fig. 5(h)). A higher sulfur
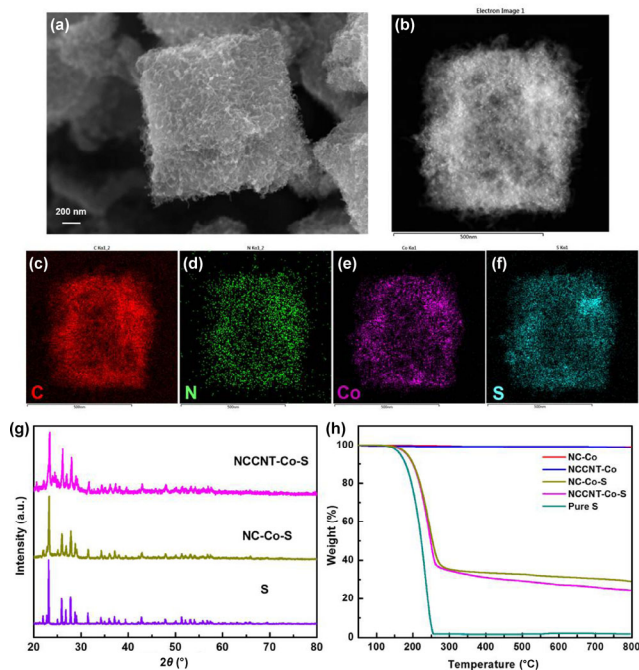
Figure 5 (a) SEM image of NCCNT-Co-S. (b)–(f) STEM image and EDX elemental mappings of C, Co, N, and S in NCCNT-Co-S. (g) XRD patterns of S, NC-Co-S, and NCCNT-Co-S. (h) TGA curves of S, NC-Co, NCCNT-Co, NC-Co-S, and NCCNT-Co-S under nitrogen atmosphere.
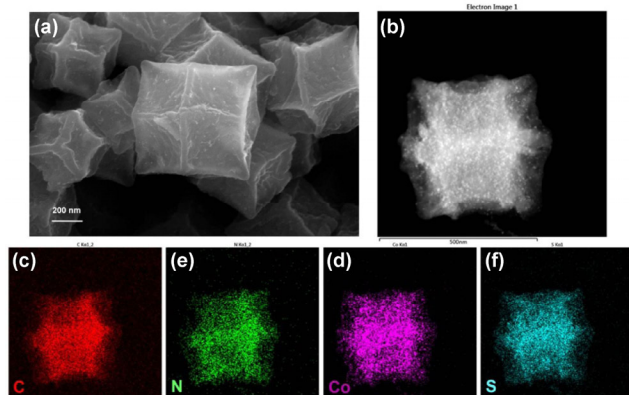

Figure 6 (a) FESEM image, (b) STEM image, and (c)–(f) EDX elemental mappings of NC-Co-S.

content was achieved within NCCNT-Co-S (76 wt.%) than NC-Co (70 wt.%), due to the larger surface area and stronger confinement resulting from the denser CNTs in NCCNT-Co-S.

The electrochemical performances of NCCNT-Co-S and NC-Co-S cathodes for Li-S batteries were evaluated by the analyses shown in Fig. 7. In order to investigate the electrochemical redox reactions during the charge/discharge process, CV curves were collected in the

potential range of 1.8–3.0 V vs. Li/Li+, at a scan rate of 0.1 mV·s−1. In the initial cathodic scan of NCCNT-Co-S (Fig. 7(a)), the reduction peak at 2.28 V corresponds to the conversion of sulfur to LiPSs (Li_2S_n, $4 < n < 8$), while another reduction peak at 2.00 V is associated with the further reduction of LiPSs to insoluble Li_2S_2 and Li_2S [26, 41–43]. In the subsequent anodic scan, the LiPSs are first produced at 2.34 V and then converted to sulfur at 2.40 V. The slight shift of the reduction and oxidation peaks after the first cycle is due to the increased viscosity of the electrolyte induced by the dissolution of LiPSs during the first cycle [12]. After the first scan, all CV curves display the typical two-step reactions in both cathodic and anodic sweeps, and the stable peaks and current intensities of NCCNT-Co-S demonstrate its superb LiPSs-trapping capacity [43, 44]. The more distinct peak at 2.40 V observed for NCCNT-Co-S than NC-Co-S indicates a more efficient oxidation of long-chain LiPSs to sulfur within NCCNT-Co-S. This can be ascribed to the effective adsorption of LiPSs and their efficient transformation to sulfur upon the co-catalyst derived from metallic Co nanoparticles and doped N [2, 43].

Galvanostatic charge/discharge tests were carried out to evaluate the lithium storage properties of the NCCNT-Co-S and NC-Co-S materials at a current density of 0.1 C (1 C = 1,675 mA·g−1). The charge/discharge profiles of NCCNT-Co-S and NC-Co-S in the first three cycles are shown in Figs. 7(c) and 7(d), respectively. Both curves display two well-defined charge/discharge plateaus, in good agreement with the CV results. The NCCNT-Co-S cathode delivers an initial specific capacity of 1,621 mAh·g−1, which is close to the theoretical capacity (1,672 mAh·g−1) of sulfur; this indicates the full utilization of sulfur, due to the homogeneous immobilization of active sulfur and the high conductivity of NCCNT-Co hosts. The capacity of the NCCNT-Co-S composite faded in the subsequent cycles, but the composite still delivered a capacity of 1,300 mAh·g−1 after three cycles. In contrast, NC-Co-S exhibits a much lower performance, with an initial discharge capacity of 1,178 mAh·g−1 and a specific capacity of 973 mAh·g−1 after three cycles. The relative large capacity fading in the first two cycles can be ascribed to the unavoidable dissolution of LiPSs in
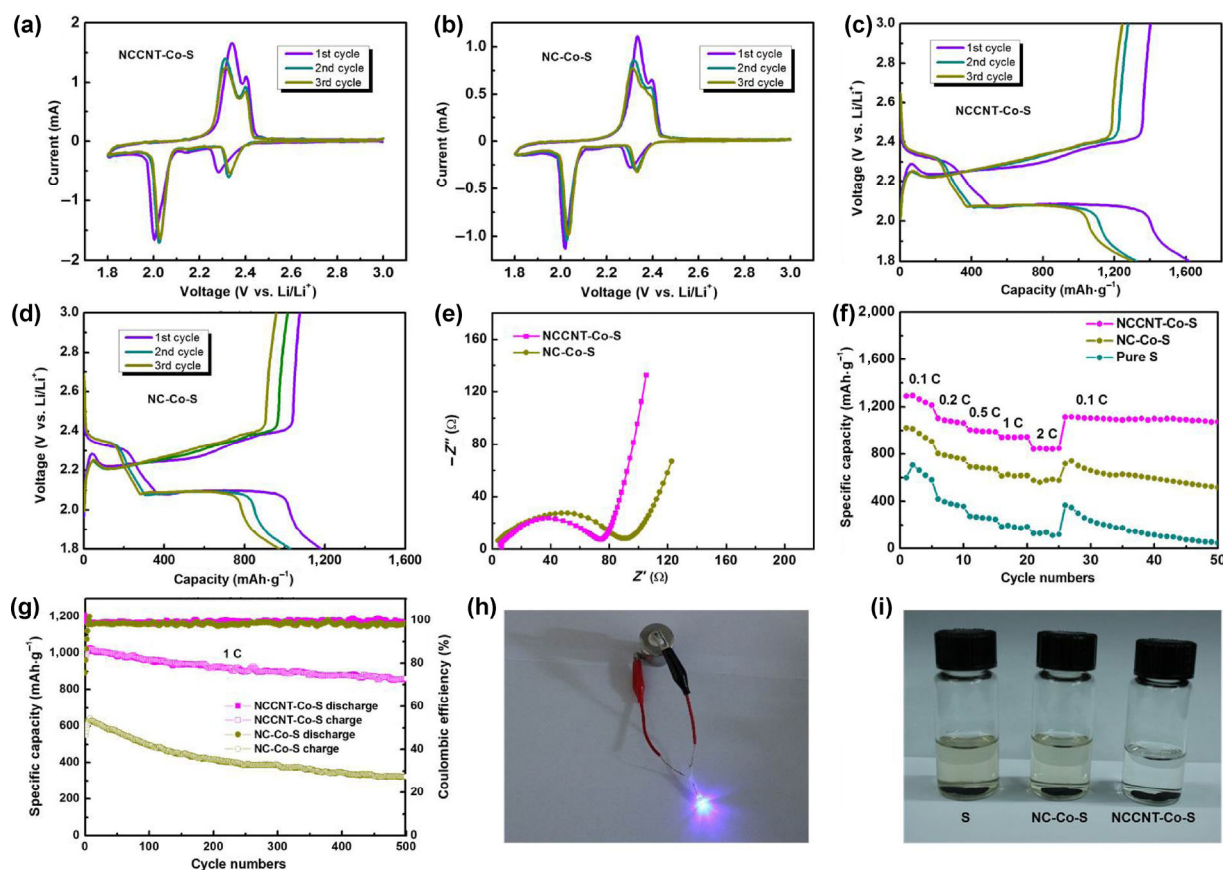
Figure 7 (a)–(d) CV plots and charge/discharge curves of NCCNT-Co-S and NC-Co-S. (e) Nyquist plots of NCCNT-Co-S and NC-Co-S cathode before cycling. (f) Rate performance of different cathodes. (g) Long-term stabilities of NCCNT-Co-S at 1 C. (h) Purple light-emitting diode (LED) powered by the assembled Li-S batteries. (i) S, NC-Co-S, and NCCNT-Co-S cathodes after cycling diluted by blank electrolyte.

the electrolyte. The discharge curves of NCCNT-Co-S and NC-Co-S exhibit slopes between 1.8 and 1.9 V, which can be ascribed to the presence of micropores in the carbon matrices that slow down the reduction of S_{2-4} to Li_2S/Li_2S_2 [45]. Compared with NC-Co-S, the internal hollow structure and larger specific surface area of NCCNT-Co-S allow a more effective interfacial contact between active sulfur and electrolyte, thus promoting the diffusion kinetics of the electrolyte. Moreover, the one-dimensional CNTs rooted on both sides of NCCNT-Co-S ensure a fast electron exchange between electrolyte and cathode. On the other hand, the internal solid structure of NC-Co-S makes it much harder for the electrolyte to react with the inner sulfur. Therefore, NCCNT-Co-S achieves superior sulfur utilization within the host due to its rationally designed nanostructure.

EIS tests were carried out to monitor the internal

resistance and charge transfer kinetics of NCCNT-Co-S and NC-Co-S cathodes. Both Nyquist plots (Fig. 7(e)) consist of depressed semicircles in the high-frequency region and sloping lines at low frequencies. The diameter of the semicircle reflects the charge transfer resistance (R_{ct}), while the inclined line is associated with the mass transfer resistance [7, 30]. Despite its higher sulfur loading, NCCNT-Co-S exhibits a lower R_{ct} (69 Ω) than NC-Co-S (91 Ω), indicating higher electrical conductivity and faster ion diffusion within the NCCNT-Co-S cathode. The reduced R_{ct}, which originates from the presence of numerous interconnected CNTs on both sides of the hollow carbon polyhedron matrix, can provide an efficient conductive framework for the electrochemical reactions and ensure a higher utilization of active sulfur. For further comparison, the rate capabilities of NCCNT-Co-S, NC-Co-S, and neat S were evaluated at various

current densities (Fig. 7(f)). Pure S exhibits a poor rate capability with fast capacity decay. For NCCNT-Co-S, specific capacities of 1,212, 1,103, 986, 943, and 845 mAh·g^{-1} are obtained at current densities of 0.1 C, 0.2 C, 0.5 C, 1 C, and 2 C, respectively. A stable capacity of 1,112 mAh·g^{-1} is recovered when the current density is switched back to 0.1 C, indicating an excellent structural stability of NCCNT-Co-S during high-rate cycling. In comparison, NC-Co-S delivers capacities of only 906, 754, 672, 615, and 575 mAh·g^{-1} at 0.1 C, 0.2 C, 0.5 C, 1 C, and 2 C, respectively, showing a reduced rate capability. These results indicate that both NCCNT-Co-S and NC-S enhance the rate capability of the sulfur cathode. However, NCCNT-Co-S exhibits a superior rate performance compared with NC-Co-S, due to the physical and chemical trapping of LiPSs, along with the catalytic effects of N and Co co-doping on the conversion reactions of sulfur during the charge/discharge processes. Consequently, the intrinsic high conductivity and integrated architecture of NCCNT-Co-S allow rapid and sufficient electrochemical reactions to take place, resulting in excellent rate performances.

A long-term cycling stability with good capacity retention is a vital requirement for Li-S batteries in practical applications. The cycling performances of NCCNT-Co-S and NC-Co-S cathodes at a high current density (1 C) are compared in Fig. 7(g). The NCCNT-Co-S cathode delivers a capacity of 975 mAh·g^{-1} in the initial cycle, which then gradually increases to 1,018 mAh·g^{-1} in the subsequent cycles, as a result of the activation process. Finally, NCCNT-Co-S maintains a high specific capacity of 860 mAh·g^{-1} after 500 cycles. A high capacity retention of 88% with a Coulombic efficiency of 98.4% is then obtained, corresponding to a capacity decay of only 0.024% per cycle. Turning to the NC-Co-S cathode, its initial capacity is 550 mAh·g^{-1} and a capacity of only 324 mAh·g^{-1} is obtained after 500 cycles, corresponding to a lower retention (62%) compared with NCCNT-Co-S. Both the specific capacity and capacitance retention of NCCNT-Co-S are much higher than those of NC-Co-S. Table S1 in the ESM shows a comparison of the performance of the present and other MOF-derived carbon cathodes reported in the literature. Figure 7(h) and Fig. S4 in the ESM show a LED powered for more than 60 min by a

battery assembled with a NCCNT-Co-S cathode and a Li anode. To investigate the effects of LiPSs adsorption in a more direct way, NCCNT-Co-S, NC-Co-S, and neat S cathodes were collected after 50 cycles and dissolved into a blank electrolyte. As shown in Fig. 7(i), the solvents of both neat S and NC-Co-S electrodes show a light gold color, which indicate that parts of LiPSs have been dissolved into the blank electrolyte. In contrast, the electrolyte of the NCCNT-Co-S electrode remains clear and lucid, indicating that the LiPSs are mainly located inside the matrix of the NCCNT-Co host. These results suggest that the different cathodes have different absorbabilities of LiPSs, with the NCCNT-Co-S cathode showing the highest absorbability. The good suppression of LiPSs dissolution in the NCCNT-Co-S cathode is due to the strong interactions between LiPSs and NCCNT-Co. When used as sulfur host, the mesopores created by the *in situ*-grown intertwined CNTs arrays, along with the hierarchical porous carbon matrix of NCCNT-Co, can physically trap the LiPSs during the charge/discharge processes. In addition, the homogenously dispersed N-doping sites and Co nanoparticles can enhance the chemical adsorption of the LiPSs. Therefore, NCCNT-Co-S can trap LiPSs through both physical and chemical interactions. Considering that the N-doping sites and Co nanoparticles also exist within NC-Co-S, it can be proposed that the N-doped CNT arrays and the porous structure of NCCNT-Co play important roles in the LiPSs trapping process. Compared with NC-Co, NCCNT-Co has a more hierarchical structure with a higher specific surface area, and the presence of dense CNTs along with the hollow structure can further enhance the contact between LiPSs and the host, thus providing a better LiPSs-trapping capability. The fine structure and composition of NCCNT-Co ensure the presence of LiPSs mostly within the electrochemical active cathode and inhibit the shuttle effect of LiPSs, thus achieving long-term cycling stability.

Based on the above discussion, the excellent performance of NCCNT-Co-S as cathode material can be explained as follows. First, the interconnected N-doped CNTs on both sides of the hollow carbon polyhedron matrix can form an integrated conductive network, which allows fast transport of electrons/ions

inside the cathode, and ensures sufficient utilization of sulfur. Second, the mesoporous structure derived from the dense CNT arrays, along with the homogeneously dispersed N-doping sites and Co nanoparticles, can efficiently trap LiPSs via physical confinement and chemical interactions. Third, co-doping by N and Co elements can significantly enhance the redox reactions of sulfur. Finally, the hierarchical porous structure of NCCNT-Co-S is beneficial for a fast mass transport and can buffer the huge volume change occurring during the rapid charge/discharge processes. All these advantages may contribute to overcome the drawbacks of Li-S batteries and thus help achieving superb energy storage performances.

4 Conclusions

In summary, we designed and prepared a unique integrated nanostructure, consisting of cobalt nanoparticle-containing porous carbon polyhedra with a N-doped carbon nanotube backbone. ZIF-67 precursors served as self-templates for the formation of the hollow carbon polyhedron matrix as well as carbon and nitrogen sources for growing N-doped CNT arrays *in situ*. The sulfur host can effectively trap LiPSs, while accelerating their electrochemical reaction kinetics at the same time. Benefiting from the high conductivity and protective effects of the CNT arrays, the obtained NCCNT-Co-S hybrid delivers high reversible specific capacity (860 mAh·g^{-1}) after 500 cycles at 1 C, high Coulombic efficiency (98.4%), good rate capability, and high capacity retention over 500 cycles. This strategy may provide new insights into the rational design and fabrication of hierarchical MOF-derived cathodes with unique nanostructures for high-performance Li-S batteries.

Acknowledgements

Electronic Supplementary Material: Supplementary material (SEM and TEM images of ZIF67; TGA curves of ZIF67; Raman spectra of NCCNT-Co and NC-Co; digital images of lightened LED; performance comparisons) is available in the online version of this article at https://doi.org/ 10.1007/s12274-018-2130-9.

References

[1] Pang, Q.; Liang, X.; Kwok, C. Y.; Nazar, L. F. Advances in lithium-sulfur batteries based on multifunctional cathodes and electrolytes. *Nat. Energy* **2016**, *1*, 16132.

[2] Li, Y. J.; Fan, J. M.; Zheng, M. S.; Dong, Q. F. A novel synergistic composite with multi-functional effects for high-performance Li-S batteries. *Energy Environ. Sci.* **2016**, *9*, 1998–2004.

[3] Manthiram, A.; Chung, S. H.; Zu, C. X. Lithium-sulfur batteries: Progress and prospects. *Adv. Mater.* **2015**, *27*, 1980–2006.

[4] Xiao, J.; Hu, J. Z.; Chen, H. H.; Vijayakumar, M.; Zheng, J. M.; Pan, H. L.; Walter, E. D.; Hu, M.; Deng, X. C.; Feng, J. et al. Following the transient reactions in lithium-sulfur batteries using an *in situ* nuclear magnetic resonance technique. *Nano Lett.* **2015**, *15*, 3309–3316.

[5] Zhao, T.; Ye, Y. S.; Peng, X. Y.; Divitini, G.; Kim, H. K.; Lao, C. Y.; Coxon, P. R.; Xi, K.; Liu, Y. J.; Ducati, C. et al. Advanced lithium-sulfur batteries enabled by a bio-inspired polysulfide adsorptive brush. *Adv. Funct. Mater.* **2016**, *26*, 8418–8426.

[6] Chung, S. H.; Manthiram, A. A polyethylene glycol-supported microporous carbon coating as a polysulfide trap for utilizing pure sulfur cathodes in lithium-sulfur batteries. *Adv. Mater.* **2014**, *26*, 7352–7357.

[7] Fang, R. P.; Zhao, S. Y.; Hou, P. X.; Cheng, M.; Wang, S. G.; Cheng, H. M.; Liu, C.; Li, F. 3D interconnected electrode materials with ultrahigh areal sulfur loading for Li-S batteries. *Adv. Mater.* **2016**, *28*, 3374–3382.

[8] Wei Seh, Z.; Li, W. Y.; Cha, J. J.; Zheng, G. Y.; Yang, Y.; Mcdowell, M. T.; Hsu, P. C.; Cui, Y. Sulphur-TiO$_2$ yolk-shell nanoarchitecture with internal void space for long-cycle lithium-sulphur batteries. *Nat. Commun.* **2013**, *4*, 1331.

[9] Chung, S. H.; Han, P.; Singhal, R.; Kalra, V.; Manthiram, A. Electrochemically stable rechargeable lithium-sulfur batteries with a microporous carbon nanofiber filter for polysulfide.

Adv. Energy Mater. **2015**, *5*, 1500738.

[10] Ma, L.; Hendrickson, K. E.; Wei, S. Y.; Archer, L. A. Nanomaterials: Science and applications in the lithium–sulfur battery. *Nano Today* **2015**, *10*, 315–338.

[11] Yang, Y.; Zheng, G. Y.; Cui, Y. Nanostructured sulfur cathodes. *Chem. Soc. Rev.* **2013**, *42*, 3018–3032.

[12] Peng, H. J.; Huang, J. Q.; Zhao, M. Q.; Zhang, Q.; Cheng, X. B.; Liu, X. Y.; Qian, W. Z.; Wei, F. Nanoarchitectured graphene/CNT@porous carbon with extraordinary electrical conductivity and interconnected micro/mesopores for lithium-sulfur batteries. *Adv. Funct. Mater.* **2014**, *24*, 2772–2781.

[13] Zhu, L.; Peng, H. J.; Liang, J. Y.; Huang, J. Q.; Chen, C. M.; Guo, X. F.; Zhu, W. C.; Li, P.; Zhang, Q. Interconnected carbon nanotube/graphene nanosphere scaffolds as free-standing paper electrode for high-rate and ultra-stable lithium–sulfur batteries. *Nano Energy* **2015**, *11*, 746–755.

[14] Yu, H. J.; Li, H. W.; Yuan, S. Y.; Yang, Y. C.; Zheng, J. H.; Hu, J. H.; Yang, D.; Wang, Y. G.; Dong, A. G. Three-dimensionally ordered, ultrathin graphitic-carbon frameworks with cage-like mesoporosity for highly stable Li-S batteries. *Nano Res.* **2017**, *10*, 2495–2507.

[15] Li, H. P.; Sun, L. C.; Zhang, Y. G.; Tan, T. Z.; Wang, G. K.; Bakenov, Z. Enhanced cycle performance of Li/S battery with the reduced graphene oxide/activated carbon functional interlayer. *J. Energy Chem.* **2017**, *26*, 1276–1281.

[16] Song, J. X.; Xu, T.; Gordin, M. L.; Zhu, P. Y.; Lv, D. P.; Jiang, Y. B.; Chen, Y. S.; Duan, Y. H.; Wang, D. H. Nitrogen-doped mesoporous carbon promoted chemical adsorption of sulfur and fabrication of high-areal-capacity sulfur cathode with exceptional cycling stability for lithium-sulfur batteries. *Adv. Funct. Mater.* **2014**, *24*, 1243–1250.

[17] Qiu, Y. C.; Li, W. F.; Zhao, W.; Li, G. Z.; Hou, Y.; Liu, M. N.; Zhou, L. S.; Ye, F. M.; Li, H. F.; Wei, Z. H. et al. High-rate, ultralong cycle-life lithium/sulfur batteries enabled by nitrogen-doped graphene. *Nano Lett.* **2014**, *14*, 4821–4827.

[18] Zhou, G. M.; Zhao, Y. B.; Manthiram, A. Dual-confined flexible sulfur cathodes encapsulated in nitrogen-doped double-shelled hollow carbon spheres and wrapped with graphene for Li-S batteries. *Adv. Energy Mater.* **2015**, *5*, 1402263.

[19] Hernández-Rentero, C.; Córdoba, R.; Moreno, N.; Caballero, A.; Morales, J.; Olivares-Marín, M.; Gómez-Serrano, V. Low-cost disordered carbons for Li/S batteries: A high-performance carbon with dual porosity derived from cherry pits. *Nano Res.* **2018**, *11*, 89–100.

[20] Xiao, Z. B.; Yang, Z.; Wang, L.; Nie, H. G.; Zhong, M. E.; Lai, Q. Q.; Xu, X. J.; Zhang, L. J.; Huang, S. M. A lightweight TiO$_2$/graphene interlayer, applied as a highly effective polysulfide absorbent for fast, long-life lithium-sulfur

batteries. *Adv. Mater.* **2015**, *27*, 2891–2898.

[21] Patil, S. B.; Kim, H. J.; Lim, H.; Oh, S. M.; Kim, J.; Shin, J.; Kim, H.; Choi, J. W.; Hwang, S. Exfoliated 2D lepidocrocite titanium oxide nanosheets for high sulfur content cathodes with highly stable Li-S battery performance. *ACS Energy Lett.* **2018**, *3*, 412–419.

[22] Chen, T.; Ma, L. B.; Cheng, B. R.; Chen, R. P.; Hu, Y.; Zhu, G. Y.; Wang, Y. R.; Liang, J.; Tie, Z. X.; Liu, J. et al. Metallic and polar Co$_9$S$_8$ inlaid carbon hollow nanopolyhedra as efficient polysulfide mediator for lithium−sulfur batteries. *Nano Energy* **2017**, *38*, 239–248.

[23] Ji, X. L.; Lee, K. T.; Nazar, L. F. A highly ordered nano-structured carbon-sulphur cathode for lithium-sulphur batteries. *Nat. Mater.* **2009**, *8*, 500–506.

[24] Park, K.; Cho, J. H.; Jang, J. H.; Yu, B. C.; De La Hoz, A. T.; Miller, K. M.; Ellison, C. J.; Goodenough, J. B. Trapping lithium polysulfides of a Li-S battery by forming lithium bonds in a polymer matrix. *Energy Environ. Sci.* **2015**, *8*, 2389–2395.

[25] Liang, X.; Rangom, Y.; Kwok, C. Y.; Pang, Q.; Nazar, L. F. Interwoven Mxene nanosheet/carbon-nanotube composites as Li-S cathode hosts. *Adv. Mater.* **2017**, *29*, 1603040.

[26] Liu, X.; Huang, J. Q.; Zhang, Q.; Mai, L. Q. Nanostructured metal oxides and sulfides for lithium–sulfur batteries. *Adv. Mater.* **2017**, *29*, 1601759.

[27] Wu, H. B.; Wei, S. Y.; Zhang, L.; Xu, R.; Hng, H. H.; Lou, X. W. D. Embedding sulfur in MOF-derived microporous carbon polyhedrons for lithium-sulfur batteries. *Chem. —Eur. J.* **2013**, *19*, 10804–10808.

[28] Xi, K.; Cao, S. A.; Peng, X. Y.; Ducati, C.; Vasant Kumar, R.; Cheetham, A. K. Carbon with hierarchical pores from carbonized metal-organic frameworks for lithium sulphur batteries. *Chem. Commun.* **2013**, *49*, 2192–2194.

[29] Bai, L. Y.; Chao, D. L.; Xing, P. Y.; Tou, L. J.; Chen, Z.; Jana, A.; Shen, Z. X.; Zhao, Y. L. Refined sulfur nanoparticles immobilized in metal-organic polyhedron as stable cathodes for Li-S battery. *ACS Appl. Mater. Interfaces* **2016**, *8*, 14328–14333.

[30] Li, Z. Q.; Li, C. X.; Ge, X. L.; Ma, J. Y.; Zhang, Z. W.; Li, Q.; Wang, C. X.; Yin, L. W. Reduced graphene oxide wrapped MOFs-derived cobalt-doped porous carbon polyhedrons as sulfur immobilizers as cathodes for high performance lithium sulfur batteries. *Nano Energy* **2016**, *23*, 15–26.

[31] He, J. R.; Chen, Y. F.; Lv, W. Q.; Wen, K. C.; Xu, C.; Zhang, W. L.; Li, Y. R.; Qin, W.; He, W. D. From metal-organic framework to Li$_2$S@C-Co-N nanoporous architecture: A high-capacity cathode for lithium-sulfur batteries. *ACS Nano* **2016**, *10*, 10981–10987.

[32] Qiu, Y. C.; Li, G. Z.; Hou, Y.; Pan, Z. H.; Li, H. F.; Li, W. F.; Liu, M. N.; Ye, F. M.; Yang, X. W.; Zhang, Y. G. Vertically aligned carbon nanotubes on carbon nanofibers: A hierarchical three-dimensional carbon nanostructure for high-energy flexible supercapacitors. *Chem. Mater.* **2015**, *27*, 1194–1200.

[33] Zhang, R. Z.; He, S. J.; Lu, Y. Z.; Chen, W. Fe, Co, N-functionalized carbon nanotubes *in situ* grown on 3D porous N-doped carbon foams as a noble metal-free catalyst for oxygen reduction. *J. Mater. Chem. A* **2015**, *3*, 3559–3567.

[34] Sun, J. K.; Xu, Q. Functional materials derived from open framework templates/precursors: Synthesis and applications. *Energy Environ. Sci.* **2014**, *7*, 2071–2100.

[35] Xia, B. Y.; Yan, Y.; Li, N.; Wu, H. B.; Lou, X. W. D.; Wang, X. A metal-organic framework-derived bifunctional oxygen electrocatalyst. *Nat. Energy* **2016**, *1*, 15006.

[36] Gulzar, U.; Li, T.; Bai, X.; Colombo, M.; Ansaldo, A.; Marras, S.; Prato, M.; Goriparti, S.; Capiglia, C.; Proietti Zaccaria, R. Nitrogen-doped single-walled carbon nanohorns as a cost-effective carbon host toward high-performance lithium-sulfur batteries. *ACS Appl. Mater. Interfaces* **2018**, *10*, 5551–5559.

[37] Chen, J. J.; Yuan, R. M.; Feng, J. M.; Zhang, Q.; Huang, J. X.; Fu, G.; Zheng, M. S.; Ren, B.; Dong, Q. F. Conductive lewis base matrix to recover the missing link of Li$_2$S$_8$ during the sulfur redox cycle in Li-S battery. *Chem. Mater.* **2015**, *27*, 2048–2055.

[38] Song, J. X.; Gordin, M. L.; Xu, T.; Chen, S. R.; Yu, Z. X.; Sohn, H.; Lu, J.; Ren, Y.; Duan, Y. H.; Wang, D. H. Strong lithium polysulfide chemisorption on electroactive sites of nitrogen-doped carbon composites for high-performance lithium-sulfur battery cathodes. *Angew. Chem., Int. Ed.* **2015**, *54*, 4325–4329.

[39] Xiang, Z. H.; Xue, Y. H.; Cao, D. P.; Huang, L.; Chen, J. F.; Dai, L. M. Highly efficient electrocatalysts for oxygen reduction based on 2D covalent organic polymers complexed with non-precious metals. *Angew. Chem., Int. Ed.* **2014**, *53*, 2433–2437.

[40] Zheng, J. M.; Tian, J.; Wu, D. X.; Gu, M.; Xu, W.; Wang, C. M.; Gao, F.; Engelhard, M. H.; Zhang, J. G.; Liu, J. et al. Lewis acid-base interactions between polysulfides' and metal organic framework in lithium sulfur batteries. *Nano Lett.* **2014**, *14*, 2345–2352.

[41] Chen, T.; Cheng, B. R.; Zhu, G. Y.; Chen, R. P.; Hu, Y.; Ma, L. B.; Lv, H. L.; Wang, Y. R.; Liang, J.; Tie, Z. X. et al. Highly efficient retention of polysulfides in "sea urchin"-like carbon nanotube/nanopolyhedra superstructures as cathode material for ultralong-life lithium-sulfur batteries. *Nano Lett.* **2017**, *17*, 437–444.

[42] Tang, C.; Zhang, Q.; Zhao, M. Q.; Huang, J. Q.; Cheng, X. B.; Tian, G. L.; Peng, H. J.; Wei, F. Nitrogen-doped aligned carbon nanotube/graphene sandwiches: Facile catalytic growth on bifunctional natural catalysts and their applications as scaffolds for high-rate lithium-sulfur batteries. *Adv. Mater.* **2014**, *26*, 6100–6105.

[43] Tan, J.; Liu, D. N.; Xu, X.; Mai, L. Q. *In situ/operando* characterization techniques for rechargeable lithium-sulfur batteries: A review. *Nanoscale* **2017**, *9*, 19001–19016.

[44] Qie, L.; Manthiram, A. A facile layer-by-layer approach for high-areal-capacity sulfur cathodes. *Adv. Mater.* **2015**, *27*, 1694–1700.

[45] Li, Z.; Jiang, Y.; Yuan, L. X.; Yi, Z. Q.; Wu, C.; Liu, Y.; Strasser, P.; Huang, Y. H. A highly ordered meso@microporous carbon-supported sulfur@smaller sulfur core-shell structured cathode for Li-S batteries. *ACS Nano* **2014**, *8*, 9295–9303.